Critical Influence of Carbon Nitride Self-assembly Coating on the Electrochemical Performance of SnO_2-TiO_2 Nanocomposite Anode Material for Lithium Ion Battery

Yangang Wang, Xiang Ding, Lihua Huang, Yangling Xu, Yuanhui Zuo, Shifei Kang[*], Lifeng Cui[*]

Department of Environmental Science and Engineering, University of Shanghai for Science and Technology, Shanghai 200093, China
[*]E-mail: sfkang@usst.edu.cn (S.F. Kang), lifeng.cui@gmail.com (L.F. Cui).

Graphitic carbon nitride (g-C_3N_4) coated SnO_2-TiO_2 nanocomposite was prepared by simple self-assembly deposition of g-C_3N_4 nanosheets on synthesized SnO_2-TiO_2 nanocomposite. Scanning electron microscopy reveals that g-C_3N_4 was uniformly coated on SnO_2-TiO_2 nanoparticles. The SnO_2-TiO_2-C_3N_4 nanocomposite was used as high capacity anode material for lithium ion battery and displayed remarkable higher capacity (380.2 mAh/g) compared to both pure SnO_2 (51.6 mAh/g) and SnO_2-TiO_2 nanocomposite (114.1 mAh/g) at 0.2C rate after 20 cycles. Rate test of SnO_2-TiO_2-C_3N_4 nanocomposite implied a slight fading of specific discharge capacities from 490 mAhg^{-1} to 330 mAhg^{-1} at current rate range of 0.1-0.5C. The significantly improved electrochemical properties of SnO_2-TiO_2-C_3N_4 nanocomposites can be attributed to g-C_3N_4 coating treatment, which not only enhanced the stability of the solid-electrolyte-interface (SEI) film but also act as a buffer layer for the large volume change of SnO2-TiO2 nanoparticles during lithium intercalation.

1. INTRODUCTION

Modern society is facing challenging energy and environment issues, which require significant substitution of fossil fuels with greener energy sources for electric energy generation and ground transportation. Renewable energy sources are the most suited option to this purpose, provided efficient devices for electric energy storage and delivery are developed. At the moment, due to their versatility and scalability, lithium-ion batteries represent the best option of electric energy storage both for portable electronics and for transportation [1]. Remarkable efforts have been devoted to expand the

application of lithium ion batteries (LIBs) to electrical vehicles, grid energy storage, and other large power applications [2]. Development of LIBs with high energy density, stable cycle life and fast charging/discharging rate performance is in great demand in order to broaden their applications in large power devices. As the electrochemical performance of LIBs is governed by the physicochemical properties of the electrode materials, increasing attention has been paid to designing new electrode materials [3-5].Currently, graphite is used as an anode material in commercial lithium secondary batteries. However, graphite can only provide a relatively low theoretic specific capacity of 372 mAh g^{-1} because when lithium atom is inserted between the graphene layers of graphite, a 6-carbon-ring can only hold one lithium atom forming LiC_6. Therefore higher-capacity alternatives are being actively pursued, particularly for anode materials [6, 7].

Among the promising alternative anode materials, tin oxide (SnO_2) has always been regarded as a very appealing candidate because of its high theoretical specific capacity of 782 mAh g^{-1} (according to the $Li_{4.4}Sn$ stoichiometry in the fully lithiated state), low discharge potential and low toxicity [8-10]. Many efforts have so far been made to prepare the design, synthesis and applications of SnO2 nanostructures with various morphologies as well as various structures. However, the lithium storage of SnO_2 mainly relies on the reversible alloying-dealloying reaction between lithium and Sn metal generated from the initial irreversible reduction of oxides. [11-14]. However repeated alloying-dealloying reaction causes large volume change and severe mechanical stress for the SnO_2 anode. This reaction mechanism leads to severe pulverization and loss of electrical connectivity of anode material during repeated Li alloying-dealloying process [15, 16]. TiO2, an important transition metal oxide with low cost and environmental benign nature, is becoming attractive as an anode material because of its long cycle life, high rate capability, and great safety properties [17-19]. Different phases of TiO_2 such as rutile [20], anatase [21], and TiO_2 (B) have been extensively studied as electrode materials for lithium ion batteries [22-26]. It was found that anatase TiO_2 can take lithium into the vacant sites of its crystalline structure, which can be viewed as stacking of zigzag chains of highly distorted edge-sharing TiO_6 octahedral [27], corresponding to a theoretical capacity of 167.5 mAh g^{-1} [16] and a neglectable volume change of 3-4% [28]. However, the relatively low capacity and poor cycle performance limited the application of titanium dioxide anode material. Nevertheless, because of its extraordinary low volume expansion during lithium insertion, TiO_2 has been investigated by many researchers as a buffer material for large-volume-change anodes such as Si, Sn, Fe_2O_3, and etc. In this regard, SnO_2-TiO_2 nanocomposite was one of the most promising choices of future anode materials for LIB. However, the cycle stability and rate performance of SnO_2-TiO_2 composites are still limited. Therefore, further improvement of the electrochemical performance and stability of SnO_2-TiO_2 nanocomposite was of significance for the research of renewable energy sources.

Graphitic carbon nitride (g-C_3N_4) is a layered carbon nitride polymer compound with conjugative π structure which was similar to graphite, owing to its strong covalent bonds between carbon and nitride, g-C_3N_4 is highly stable under thermal, as well as acid or base solutions corrosion. Currently, composite with g-C_3N_4 could be an ideal approach to achieve enhanced and tunable catalystsin applications such as an effective metal-free catalyst in Friedal-Crafts reaction [29], hydrogenation reaction [30], and photodegradation of dyes [31-37]. The study of g-C_3N_4 as anode

material for LIBs has also attracted extensive attention. Because of its structural stability, g-C_3N_4 was also studied extensively as a buffer material for other large-volume-change anode material.

In this regard, design and controllable synthesis of trisome nanocomposite of SnO_2, TiO_2 and g-C_3N_4 as high performance anode material for LIBs is promising. Herein, we report a g-C_3N_4 coated SnO_2-TiO_2 nanocomposite prepared by simple calcination and liquid phase self-assembly coating methods. In this trisome nanocomposite system, SnO_2 provides high capacity, whereas TiO_2 and C_3N_4 serve as both active materials and buffering materials, which can alleviate the volume expansion issue of high capacity SnO_2 anode. Compared to pure SnO_2 and SnO_2-TiO_2 composite, the SnO_2-TiO_2-C_3N_4 nanocomposite demonstrates significantly improved reversibility and cyclability, which can be attributed to the buffering effect of TiO_2 and g-C_3N_4 coating on the large-volume-change SnO_2.

2. EXPERIMENTAL

2.1. Sample preparation

All reagents were of analytical grade and were purchased from Shanghai Chemical Corp without further purification.

2.1.1 Preparation of SnO₂-TiO₂ composite

The pure SnO_2 was prepared by direct calcination of $SnCl_2 \cdot 2H_2O$ at $550^{\circ}C$. SnO_2-TiO_2 composite was prepared by a calcination method using $SnCl_2 \cdot 2H_2O$ and $TiCl_4$ as precursor. In a typical synthesis procedure, $SnCl_2 \cdot 2H_2O$ (20mmol) as the source of Sn was first dissolved in 20ml acetone to obtain clear solution under magnetic stirring. After a few minutes, TiCl4 (10mmol) was added into the dispersion and the mixture was stirred constantly at room temperature to form a homogeneous solution. Subsequently, the mixture was transferred to a clean flat Petri dish (diameter: 8cm) to evaporate the excess acetone. After that, the above mixture was put into a semi-closed alumina crucible with a cover, then it was calcined in air at $550^{\circ}C$ with a heating and cooling rate of $2^{\circ}C$ /min and maintained at this temperature for 3h to get fine crystalline SnO_2-TiO_2 composite for further investigation. The reference sample, the bare SnO_2 was also prepared in a similar process in the absence of $TiCl_4$.

2.1.2 Preparation of g-C₃N₄ nanosheets

Bulk g-C_3N_4 was prepared by a copolymerization process [38]. In a typical synthesis procedure, three grams of dicyandiamide and 0.15g of barbituric acid (BA) were mixed in 15 mL of deionized water. Then the mixture was stirred vigorously at $90^{\circ}C$ in the oil bath pan until all water was evaporated, leaving a white solid. The resulting white solids were collected, put into the muffle furnace and calcined at $550^{\circ}C$ with a heating rate of $2^{\circ}C$ /min and maintained at this temperature for 4h in air to obtain bulk g-C_3N_4. To obtain g-C_3N_4 nanosheets, the as-prepared bulk g-C_3N_4 was grounded to fine

powder and then added into methanol. After being ultrasonically treated for 30 min, bulk g-C_3N_4 was exfoliated into thin sheets and disintegrated into a homogeneous suspension.

2.1.3 Preparation of SnO₂-TiO₂-C₃N₄ nanocomposite

SnO_2-TiO_2-C_3N_4 nanocomposite was prepared by g-C_3N_4 surface coating modification of SnO_2-TiO_2. The SnO_2-TiO_2-C_3N_4 nanocomposite was fabricated via a self-assembly procedure. The above as-prepared SnO_2-TiO_2 composite was then dispersed in the g-C_3N_4 suspension and stirred at room temperature for 24h. The resultant composite powder was put into a vacuum oven and dried at 60^oC for 6h. The sample was labeled as SnO_2-TiO_2-C_3N_4 nanocomposite.

2.2. Preparation of coin cell batteries

Electrochemical properties of the SnO_2, SnO_2-TiO_2 and SnO_2-TiO_2-C_3N_4 nanocomposites were evaluated at room temperature by hand-made CR2016 coin cells with lithium metal as the counter and reference electrodes. The working electrodes were formulated from a mixture of 75wt% active material, 15wt% conducting agent (Super-P carbon black) and 15wt% polyvinylidene fluoride (PVDF) binder, which was added to N-methyl-2-pyrrolidone (NMP) to form a homogenous slurry. After mechanical stirring, the resulting slurries were immediately casted onto copper foil, dried in a vacuum oven at $120℃$ for 10h, pressed under an oil machine and then left at room temperature overnight. Metal lithium was used as counter and reference electrode, a microporous polyethylene film (Celgard 2400) as separator. The electrolyte comprises 1M $LiPF_6$ in ethyl carbonate (EC)/dimethyl carbonate (DMC)/ethylmethyl carbonate (EMC) (1:1:1 by volume). Cell assembly was carried out in a glove box recirculating with Ar in which both oxygen and moisture contents were kept below 1 ppm.

### 2.3. Materials characterization and the electrochemical measurements

The crystal structures of the as-synthesized samples were characterized by X-ray powder diffraction (XRD, Bruker D8 Advance) using Cu Kα radiation at 40kV and 40mA over a 2θ range of 10-80°. Scanning electronic microscopy (SEM, VEGA3 SBH, 10 kV) was used to observe the size and the morphology of the samples. To determine the actual amount of g-C_3N_4 in the nanocomposite,thermogravimetric (TG) analysis was carried out using a Perkin EImer Simultaneous T hermal Analyzer (STA 8000, America) from 50 to 950^0C in an air flow of 25 mL/min at a heating rate of 10 ^oC /min. Electrochemical tests were carried out by using the above coin-type half cells. Galvanostatic charge-discharge measurements were performed on a battery tester (NEWARE, China) at 0.2C and were discharged (alloying) and charged (de-alloying) over the potential range of 0.05-2.5V (versus Li/Li^+) at a scanning rate of 0.5mV s^{-1}. For the rate performance measurement, the current was varied from 0.1C to 0.5C, then back to 0.1C. All experiments were carried out at room temperature.

3. RESULTS AND DISCUSSION

The X-ray diffraction patterns of SnO_2, SnO_2-TiO_2 and SnO_2-TiO_2-C_3N_4 are shown in Fig. 1 (a) – (c), respectively. In Fig. 1 (a), all intensive diffraction peaks can be well indexed to crystalline SnO_2 (JCPDS card no. 41-1445). Also, it can be obviously observed that there is no peaks corresponding to $SnCl_2$, Sn, or other impurities. Interestingly, in Fig. 1 (b), only anatase phase TiO_2 (JCPDS card no. 21-1276) is observed and no crystal structure of SnO_2 appears, which may be assigned to two reasons: the primary reason is that the diffraction peaks positions of SnO_2 are very close to that of TiO_2, in which the high peak intensity of TiO_2 crystal can be easily achieved.
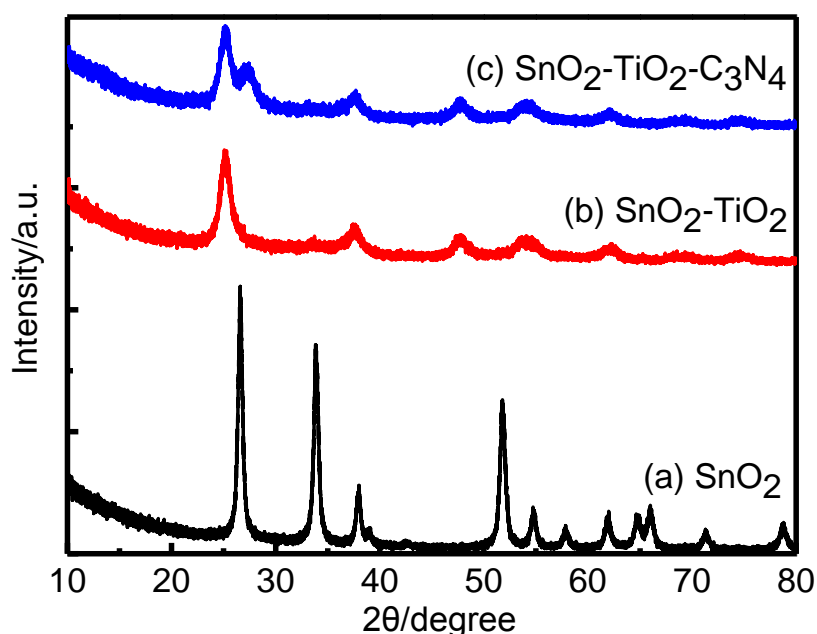
**Figure 1.** X-ray diffraction patterns of: (a) SnO_2; (b) SnO_2-TiO_2 and (c) SnO_2-TiO_2-C_3N_4 nanocomposite.
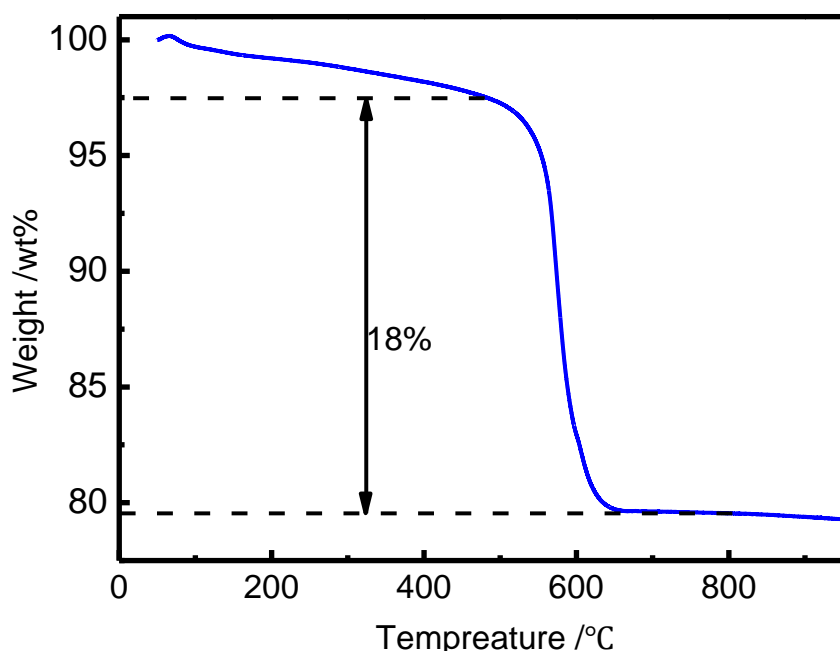
Figure 2. TG curves of the SnO_2-TiO_2-C_3N_4 nanocomposite.

The other reason is that the SnO_2 nanoparticles dispersed sufficiently during the introduction process of TiO_2, resulting in weak peak intensity of SnO_2 crystal compared with that of TiO_2. Similar results are also seen in the SnO_2-TiO_2-C_3N_4 diffraction except a peak at 27.6°, which is attributed to (002) diffraction peaks of g-C_3N_4, implying the g-C_3N_4 is successfully introduced into the composite structure after the two-step self-assembly procedure. Broadened peaks are also detected in the XRD patterns of SnO_2 and SnO_2-TiO_2-C_3N_4 nanocomposite, reflecting their decreased crystallinity and smaller crystallite dimensions.
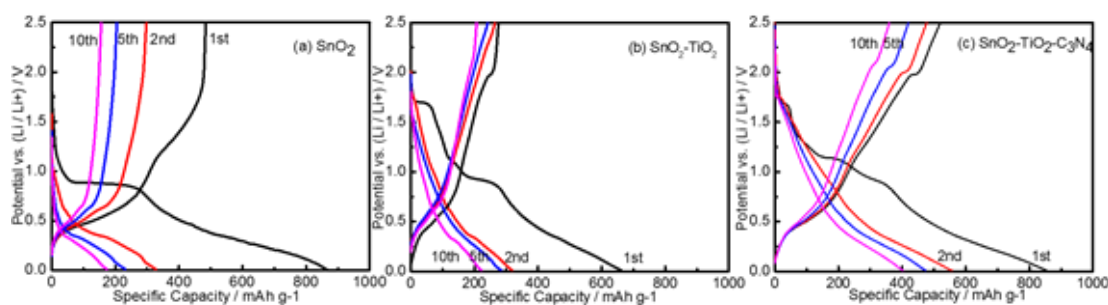
Fig. 2 shows the TG curves of the SnO_2-TiO_2-C_3N_4 nanocomposite with a heating rate of 10 ^{0}C/min from 50 to 950 ^{0}C under the air atmosphere. There are three temperature intervals where significant mass loss can be detected. The first one is the interval below 500 ^{0}C which is attributed to the evaporation of the absorbed moisture in the sample and the decomposition of the inorganic constituents of the precursor. The major weight loss takes place between 550 and 750 ^{0}C, it can be clearly seen that the weight of the SnO_2-TiO_2-C_3N_4 nanocomposite decreased rapidly. Since TiO_2 and SnO_2 are not composed in this temperature range of 550-750 ^{0}C, the weight loss corresponds to the loss of the g-C_3N_4, verifying the presence of 18wt% g-C_3N_4 in the SnO_2-TiO_2-C_3N_4 nanocomposite. In the last region, the TG curve becomes flat, indicating that the weight of the sample is stable after 750 ^{0}C and no phase transformation occurs. It can conclude that the SnO_2-TiO_2-C_3N_4 nanocomposite after calcination had high thermal stability and the g-C_3N_4 layer successfully coated on the surface of the SnO_2-TiO_2-C_3N_4 nanocomposite, which can serve as a protection layer preventing the aggregation of the nanoparticles.
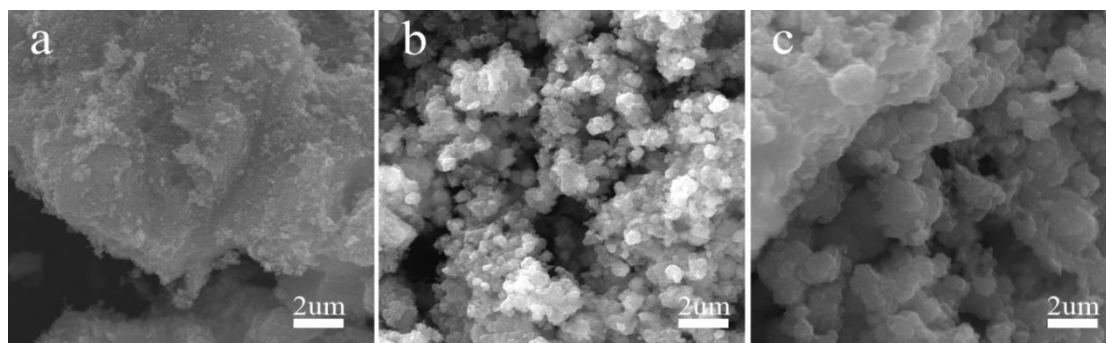
Figure 3. Representative SEM images of the as-prepared samples: (a) SnO_2; (b) SnO_2-TiO_2 and (c) SnO_2-TiO_2-C_3N_4 nanocomposite.

Surface morphologies and structures of SnO_2, SnO_2-TiO_2, and the SnO_2-TiO_2-C_3N_4 nanocomposite are presented in Fig. 3a-c, respectively. Fig. 3a shows that the pure SnO_2 sample tends to severely agglomerate without regular feature in large dimension, and no free particles could be recognized. By means of incorporating the TiO_2 in the SnO_2, as shown in the typical SEM image in Fig. 3b, SnO_2-TiO_2 nanocomposite was achieved. The as-prepared SnO_2-TiO_2 nanocomposite is composed of nanoparticles rather small and uniform with the size ranging from 0.1 to 0.25 μm in micro spherical shape, which aggregated to form bigger clusters, implying the successful introduction of TiO_2 into SnO_2-TiO_2 nanocomposite. Besides, the surface of SnO_2-TiO_2 nanocomposite becomes

coarse. Taken the preparation process and the XRD results in Fig.1 pattern (b) into account, SnO_2 particles are most possibly wrapped into TiO_2 nanoparticles, and thus the volume of change of SnO_2 during repeated charge-discharge can be largely suppressed due to the buffering effect of TiO_2 nanoparticles. Comparing Fig. 3b and Fig. 3c, it can be observed that the morphology is not significant changed via a two-step self-assembly procedure to obtain the SnO_2-TiO_2-C_3N_4 nanocomposite. But the surface of SnO_2-TiO_2-C_3N_4 nanocomposite becomes smooth, indicating that the g-C_3N_4 layer has been coated on the surface of nanoparticles homogeneously. Plenty of metal oxide nanoparticles are uniformly distributed on the surface, whereas no separate nanoparticles could be observed. Therefore, the g-C_3N_4 layer can effectively facilitate Li^+ diffusion by preventing the nanoparticles agglomerate, thus enhanced reversibility can be obtained.


Figure 4. Charge-discharge voltage profiles of (a) SnO_2, (b) SnO_2-TiO_2 and (c) SnO_2-TiO_2-C_3N_4 nanocomposite in the 1st, 2nd, 5th and 10th cycles at 0.1C.

Fig. 4 shows the charge-discharge voltage profiles of the SnO_2, SnO_2-TiO_2 and SnO_2-TiO_2-C_3N_4 nanocomposite for the 1st, 2nd, 5th and 10th cycles. The comparison of these voltage profiles of all electrodes are investigated in the range of 0-2.5V at the same rate. The initial discharge capacities of SnO_2, SnO_2-TiO_2 and SnO_2-TiO_2-C_3N_4 nanocomposites are 863 mAhg^{-1}, 662 mAhg^{-1} and 853 mAhg^{-1}, respectively. It is obviously to see that the capacity of SnO_2 is the highest which indicates that the majority of the capacity originates from the SnO_2 because of its high theoretic specific capacity. The charge capacity of the SnO_2, SnO_2-TiO_2 and SnO_2-TiO_2-C_3N_4 nanocomposites in the first cycle are 327 mAhg^{-1}, 318 mAhg^{-1} and 555 mAhg^{-1}, respectively. The irreversible capacity losses between the discharge and charge in the first cycle are taken part in all three electrodes, which can be attributed to the formation of Li_2O and solid-electrolyte interface (SEI) during the first charge/discharge process.

The initial plateau of SnO_2 in the potential range from about 1.10 to 0.50 V, corresponds to a classic conversion reaction between SnO_2 and Li^+, leading to the formation of Sn and Li_2O in the first discharge step. Regarding charge-discharge voltage profiles of (b) for SnO_2-TiO_2, two distinct regions can be observed during the first charging process. The plateau between the potential ranges of 0.50-1.10 V is exactly similar to the pure SnO_2. The other region is a plateau that can be observed at 1.75 V, which is a typical characteristic of the Li^+ insertion/extraction in TiO_2. On the other hand, for the SnO_2-TiO_2-C_3N_4 nanocomposite, apart from the discharge/charge plateaus of SnO_2 and TiO_2, there are discernible voltage plateaus above 1.0 V, which may be attributed to the introduction of the g-C_3N_4.

However, from the second cycle, it is hard to distinguish the different Li^+ insertion processes. After 10 cycles, the capacities of the SnO_2-TiO_2-C_3N_4 nanocomposite decreases slowly, whereas the capacities of the SnO_2 and SnO_2-TiO_2 undergo fast capacity decay in repeated cycling. Therefore, the SnO_2-TiO_2-C_3N_4 nanocomposite shows much slower capacity loss and obviously improved cycling performance than those of the SnO_2 and SnO_2-TiO_2, which could be related to the buffering effect of TiO_2 and the introduction of g-C_3N_4 coating layer on the huge volume change of SnO_2.
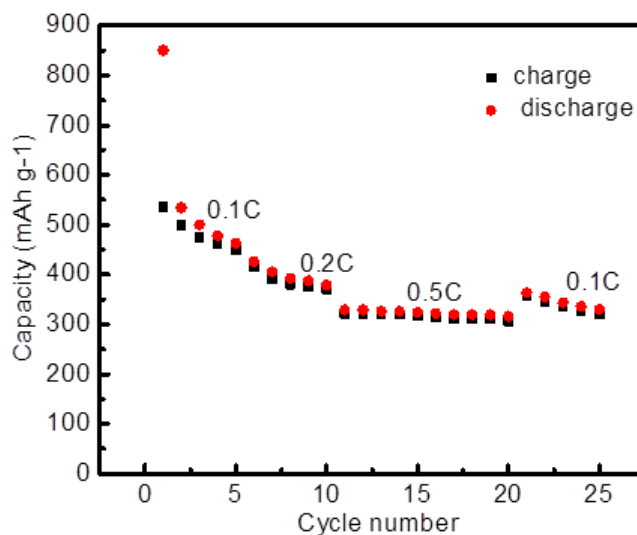
Figure 5. The rate capacity measurement of the SnO_2-TiO_2-C_3N_4 nanocomposite electrodes at different cycling rates: 1st to 5th cycles at 0.1C, 6th to 10th cycles at 0.2C, 11st to 20th cycles at 0.5C, 21st to 25th cycles at 0.1C.

In order to demonstrate the effect of the SnO_2-TiO_2-C_3N_4 nanocomposite on improving the rate capability of the electrode, the cyclic performances of the SnO_2-TiO_2-C_3N_4 nanocomposite at different current rates are shown in Fig. 5. For each stage the charge-discharge processes of the material are taken for 1st to 5th cycles at 0.1C, 6th to 10th cycles at 0.2C, 11st to 20th cycles at 0.5C, 21st to 25th cycles at 0.1C. Its specific discharge capacities of 490 mAhg^{-1} are obtained at a rate of 0.1C; this value decreases to around 390 mAhg^{-1} at 0.2C and 330 mAhg^{-1} at 0.5C. When the current density is returned back to initial 0.1C again after cycling at high current density, it is clearly to seen that the capacity recovers to about 350 mAhg^{-1}, which accounts for 71% of the initial capacity at 0.1C, indicating that the as-prepared sample can endure changes of various current densities to retain a good stability. This result confirms an improvement in the rate capacity of the material by introducing TiO_2 and g-C_3N_4 into SnO_2 via a two-step self-assembly procedure to obtain the SnO_2-TiO_2-C_3N_4 nanocomposite, which can work together to prevent the agglomeration of nanoparticles. This structure also significantly facilitates Li^+ diffusion, which improves the utilization of active SnO_2. At the same time, TiO_2 also contributes electrochemical activity in repeated cycling process.
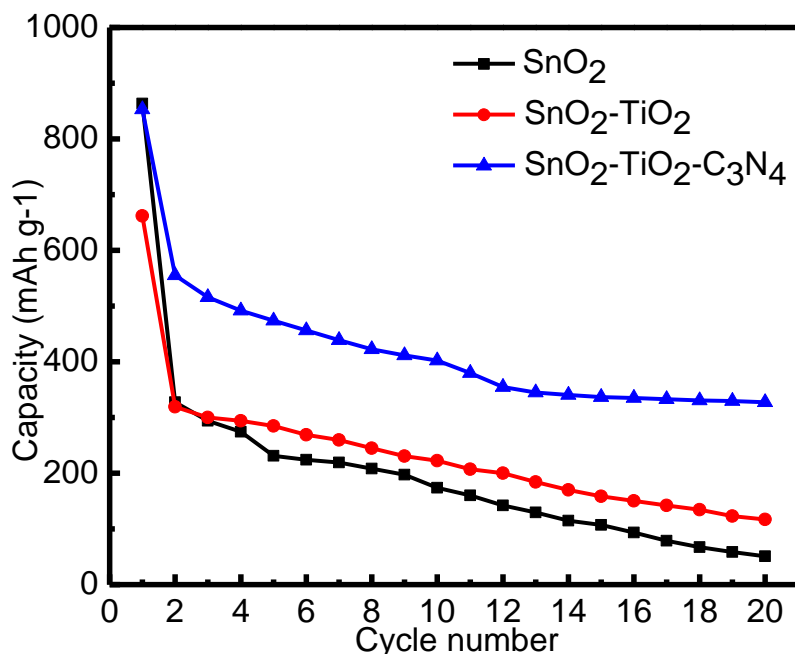
**Figure 6.** Discharge capacity versus cycle number of the coin cell with: (a) SnO_2; (b) SnO_2-TiO_2 and (c) SnO_2-TiO_2-C_3N_4 nanocomposite. The charge-discharge current rate is 0.2C and the potential range is between 0.05 and 2.5V.

Fig. 6 shows the cycling characteristics of the SnO_2, SnO_2-TiO_2 and SnO_2-TiO_2-C_3N_4 nanocomposite for 20 cycles at 0.1C between 0.5and 2.5V. A comparison of curves reveals that the cyclic performance of the SnO_2-TiO_2-C_3N_4 nanocomposite is best among all the anode materials, which shows a very stable capacity of 380.2 mAhg^{-1} over 20 cycles. The capacity retentions of the SnO_2, SnO_2-TiO_2 and SnO_2-TiO_2-C_3N_4 nanocomposite are 6%, 17% and 44% after 20 cycles, respectively. The major reason behind the poor cyclability of pure SnO_2 is the drastic volume change of electrode material caused by the still unavoidable agglomeration of SnO_2 nanoparticles during the charge-discharge cycling process. In sharp contrast, the SnO_2-TiO_2-C_3N_4 nanocomposite shows much slower capacity loss and obviously improved cycling performance than those of the SnO_2 and SnO_2-TiO_2.

In order to investigate the influence of g-C_3N_4 coating on the kinetics of Li$^+$ iron intercalation/deintercalation on the working electrodes, we carried out EIS test at voltage of 2.0 V after the first cycle. Fig. 7 shows the EIS curves of the SnO_2, SnO_2-TiO_2 and SnO_2-TiO_2-C_3N_4 electrodes. The high frequency EIS curves are composed of a depressed semicircle, which related to the charge transfer resistance at the active material interface. While the low frequency EIS curves are straight sloping line, which indicates the Warburg impedance caused by a semi-infinite diffusion of Li$^+$ in the electrode. In the equivalent circuit, Re represents the contact resistance between the working electrode and the reference electrode, Rs is the lithium diffusion resistance in the SEI film, Rct means the charge transfer resistance. In addition, CPEs is the constant phase-angle element depicting the non-ideal capacitance of the SEI film, CPEct indicate the constant charge transfer capacitance of the electrode layer, and Zw state the Warburg impedance of Li$^+$ diffusion in the SnO_2-TiO_2-C_3N_4 material. All the

EIS data were fitted using an equivalent circuit, the fitting results of Rs, Rct and CPEct of SnO_2, SnO_2-TiO_2 and SnO_2-TiO_2-C_3N_4 samples are shown in Table 1. It can be observed that the Rct values decrease largely after g-C_3N_4 coating treatment, which means that g-C_3N_4 coating layer play an important role in suppressing the charge transfer impedance of the SnO_2-TiO_2 cathode during cycling. The high value of CPEct in SnO_2 and SnO_2-TiO_2 electrode fitting results means high constant charge transfer capacitance of SnO_2 and SnO_2-TiO_2 material, which means fast serious capacity fading at high rates. In contrat, SnO_2-TiO_2-C_3N_4 samples under g--C_3N_4 coating treatment show excellent rate performance and much lower CPEct value. Therefore, it can be concluded that the improvement of the Li^+ ion diffusion in SEI and the electrochemical performance is responsible for the g-C_3N_4 coating treatment. Hence, the improved initial coulombic efficiency and cycle performance of SnO_2-TiO_2-C_3N_4 material can be attributed to the higher Li^+ transfer kinetics and the lower charge transfer resistance [39-41].
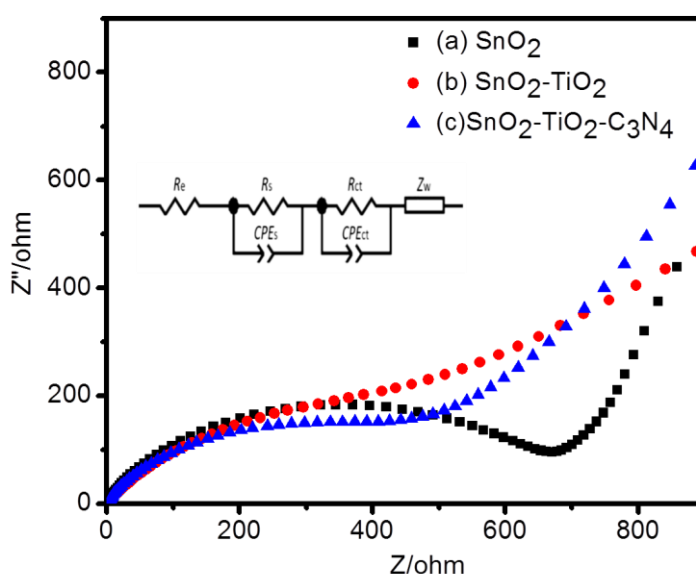
Figure 7. Electrochemical impedance spectra of (a) SnO_2; (b) SnO_2-TiO_2 and (c) SnO_2-TiO_2-C_3N_4 samples. Inset is the equivalent circuit.

Table 1. Impedance parameters of SnO_2, SnO_2-TiO_2 and SnO_2-TiO_2-C_3N_4 samples.

Sample	Rs/ohm	Rct/ohm	CPEct/uF
SnO_2	1.14	876.8	90.7
SnO_2-TiO_2	2.833	864.2	19.73
SnO_2-TiO_2-C_3N_4	2.885	110.6	5.182

Overall, the high capacity, good cycling stability, and excellent rate capability of SnO_2-TiO_2-C_3N_4 nanocomposite can be attributed to the following reasons. First, the g-C_3N_4 coating layer can serve as multidimensional pathways to facilitate the Li^+ insertion/extraction by rapid forming of steady solid-electrolyte interface. Second, our fabrication approach allows the homogeneous distribution of

SnO_2 NPs in the 3D interconnected buffer structure of TiO_2, which can effectively suppress the aggregation of inner-plane SnO_2 NPs during the charge–discharge cycles. Third, the mesopores generated by the condensed packing of g-C_3N_4, TiO_2 and SnO_2 NPs can improve the surface area of the hybrid and thus provide more active sites for the storage of lithium ion.

4. CONCLUSIONS

SnO_2-TiO_2-C_3N_4 nanocomposite was prepared by surface hybridization of SnO_2-TiO_2 with g-C_3N_4. The uniform coating of g-C_3N_4 on SnO_2-TiO_2 nanoparticles was achieved using liquid phase deposition method. The SnO_2-TiO_2-C_3N_4 nanocomposite displayed remarkable higher anode capacity (380.2 mAh/g) compared to both pure SnO_2 (51.6 mAh/g) and SnO_2-TiO_2 nanocomposite (114.1 mAh/g) at 0.2C rate after 20 cycles. The specific discharge capacities faded slightly from 490 mAhg^{-1} to 330 mAhg^{-1} at current rate range of 0.1-0.5C. The significantly enhanced electrochemical properties can be attributed to the unique buffering effect of g-C_3N_4 and TiO_2 which facilitate the Li^+ insertion/extraction during the charge–discharge cycles. Furthermore, the mesopores generated by the condensed packing of g-C_3N_4, TiO_2 and SnO_2 NPs is another contributing factor for the improved electrochemistry performance by provide more active sites for the storage of lithium ion. This approach provides a new pathway for g-C_3N_4-based composite material, which can be expanded in the application in lithium-ion batteries.

References

1. V. Etacheri, R. Marom, R. Elazari, G. Salitra and D. Aurbach, *Energy & Environmental Science*, 4 (2011) 3243.
2. B. Kang and G. Ceder, *Nature*, 458 (2009) 190-193.
3. L.J. Fu, H. Liu, H.P. Zhang, C. Li, T. Zhang, Y.P. Wu, R. Holze and H.Q. Wu, *Electrochemistry Communications*, 8 (2006) 1-4.
4. J.S. Chen, L.A. Archer and X. Wen Lou, *Journal of Materials Chemistry*, 21 (2011) 9912.
5. Z. Wang, L. Zhou and X.W. David Lou, *Advanced Materials*, 24 (2012) 1903-1911.
6. R.A. Huggins, *Journal of Power Sources*, 81-82 (1999) 13-19.
7. J.O.B. M. Winter, M. Spahr and P. Novak, *Advanced Materials*, 10 (1998) 725-763.
8. C. Wang, G. Du, K. Ståhl, H. Huang, Y. Zhong and J.Z. Jiang, *Journal of Physical Chemistry C*, 116 (2012) 4000-4011.
9. Z. Wang, D. Luan, F.Y. Boey and X.W. Lou, *Journal of the American Chemical Society*, 133 (2011) 4738-4741.
10. E.Y. Seung-Min Paek, and Itaru Honma, *Nano letters*, 9 (2009) 72-75.
11. L. Ji, Z. Lin, M. Alcoutlabi and X. Zhang, *Energy & Environmental Science*, 4 (2011) 2682.
12. H. Wang, and A.L. Rogach, *Chemistry of Materials*, 26 (2014) 123.

13. Li-lai Liu, Mao-zhong An, Pei-xia Yang and Jin-qiu Zhang, *International Journal of Electrochemical Science*, 10 (2015) 4461 – 4472.

14. Lili Feng, Zhewen Xuan, Siping Ji, Weiru Min, Hongbo Zhao and Hui Gao, *International Journal of Electrochemical Science,* 10 (2015) 2370 – 2376.

15. Z. Yang, G. Du, C. Feng, S. Li, Z. Chen, P. Zhang, Z. Guo, X. Yu, G. Chen, S. Huang and H. Liu, *Electrochimica Acta*, 55 (2010) 5485-5491.

16. J.S. Chen and X.W. Lou, *Materials Today*, 15 (2012) 246-254.

17. D.C. Dong, hai Wang, Juan Li, Zhenguo Yang, Zimin Nie, Rong Kou, Dehong Hu, Chongmin Wang, Laxmikant V. Saraf, Jiguang Zhang, Ilhan A. Aksay and Jun Liu, *ACS Nano*, 3 (2009) 907-914.

18. S. Yang, X. Feng and K. Mullen, *Advanced Materials*, 23 (2011) 3575-3579.

19. J.-Y. Shin, D. Samuelis and J. Maier, *Advanced Functional Materials*, 21 (2011) 3464-3472.

20. Y.S. Hu, L. Kienle, Y.G. Guo and J. Maier, *Advanced Materials*, 18 (2006) 1421-1426.

21. Y.G. Guo, Y.S. Hu, W. Sigle and J. Maier, *Advanced Materials*, 19 (2007) 2087-2091.

22. Y. Ren, Z. Liu, F. Pourpoint, A.R. Armstrong, C.P. Grey and P.G. Bruce, *Angewandte Chemie. International Ed. in English*, 51 (2012) 2164-2167.

23. S. Liu, H. Jia, L. Han, J. Wang, P. Gao, D. Xu, J. Yang and S. Che, *Advanced Materials*, 24 (2012) 3201-3204.

24. H. Liu, Z. Bi, X.G. Sun, R.R. Unocic, M.P. Paranthaman, S. Dai and G.M. Brown, *Advanced Materials*, 23 (2011) 3450-3454.

25. A.G. Dylla, P. Xiao, G. Henkelman and K.J. Stevenson, *Journal of Physical Chemistry Letters*, 3 (2012) 2015-2019.

26. K. Shin, H.J. Kim, J.M. Choi, Y.M. Choi, M.S. Song and J.H. Park, *Chemical communications (Cambridge, England)*, 49 (2013) 2326-2328.

27. K.Y.a.T.Y. Gerhard Nuspl, *Journal of Materials Chemistry*, 7 (1997) 2529-2536.

28. M.M. Rahman, J.-Z. Wang, M.F. Hassan, D. Wexler and H.K. Liu, *Advanced Energy Materials*, 1 (2011) 212-220.

29. F. Goettmann, A. Fischer, M. Antonietti and A. Thomas, *Chemical Communications*, (2006) 4530.

30. Y. Wang, J. Yao, H. Li, D. Su and M. Antonietti, *Journal of the American Chemical Society*, 133 (2011) 2362-2365.

31. S.C. Yan, Z.S. Li, Z.G. Zou, *Langmuir*, 25 (2009) 10397-10401.

32. S.C. Yan, S.B. Lv, Z.S. Li and Z.G. Zou, *Dalton Transactions*, 39 (2010) 1488-1491.

33. S.C. Yan, Z.S. Li and Z.G. Zou, *Langmuir*, 26 (2010) 3894-3901.

34. Y. Guo, S. Chu, S. Yan, Y. Wang and Z. Zou, *Chemical communications (Cambridge, England)*, 46 (2010) 7325-7327.

35. Y. Zhang and M. Antonietti, *Chemistry-an Asian Journal*, 5 (2010) 1307-1311.

36. M. Doblinger, B.V. Lotsch, J. Wack, J. Thun, J. Senker and W. Schnick*, Chemical communications (Cambridge, England)*, (2009) 1541-1543.

37. Y. Zhang, A. Thomas, M. Antonietti and X. Wang, *Journal of the American Chemical Society*, 131 (2008) 50-51.

38. J. Zhang, X. Chen, K. Takanabe, K. Maeda, K. Domen, J.D. Epping, X. Fu, M. Antonietti and X. Wang, *Angewandte Chemie. International Ed. in English*, 49 (2010) 441-444.

39. A.Y. Shenouda and K. Murali, *Journal of Power Sources*, 176 (2008) 332-339.

40. Y. Yu, J.J Zhang and L.G Xue, *Journal of Power Sources*, 196 (2011) 10240-10243.

41. K. Wijeratne, J. Akilavasan and M. Thelakkat, *Electrochimica Acta*, 72 (2012) 192-198.